KSME

Springer

Journal of Mechanical Science and Technology 35 (2) 2021

Original Article
DOI 10.1007/s12206-021-0104-4

Keywords:
· Ball-screw system
· Coupling vibration
· Frequency response
· Hybrid model
· Ritz series

Correspondence to:
Qin Wu
qwu.1973@hotmail.com

Citation:
Wu, Q., Gu, F., Ball, A., Huang, H. (2021). Hybrid model for the analysis of the modal properties of a ball screw vibration system. Journal of Mechanical Science and Technology 35 (2) (2021) 461~470.
http://doi.org/10.1007/s12206-021-0104-4

Received May 7th, 2020
Revised October 8th, 2020
Accepted October 29th, 2020

† Recommended by Editor
No-cheol Park

Hybrid model for the analysis of the modal properties of a ball screw vibration system

Qin Wu[1,2], Fengshou Gu[2], Andrew Ball[2] and Hua Huang[1]

[1]School of Mechanical and Electrical Engineering, Lanzhou University of Technology, Lanzhou 730050, China, [2]Centre for Efficiency and Performance Engineering, University of Huddersfield, Huddersfield HD1 3DH, UK

Abstract In accordance with the vibration characteristics of ball screw feed systems, a hybrid modeling method is proposed to study its dynamic behavior. Partially, the ball screw is modeled as a continuous body, and the remaining components are considered lumped masses, allowing for a realistic description of the dynamics of the feed system. The axial, torsional, transverse, and bending vibration models of a ball screw carriage system are established via the Rayleigh-Ritz series method based on the Timoshenko beam assumption. The established model that added the Timoshenko beam assumption obtains the coupling vibration displacement between the transverse and bending vibrations of the lead screw, which is close to real situations. Numerical simulations are conducted to investigate the changes of the natural frequency and modal shapes of ball screw systems with carriage positions. Results show that the carriage position has significant influence on the amplitude and direction of axial and transverse vibrations, substantial influence on the direction of the bending vibration, and minimal influence on the amplitude and direction of torsional vibration. These results indicate that the proposed hybrid model performs well to predict the vibration characteristics of the feed system. Moreover, the carriage position and carriage load also have a remarkable effect on the frequency response of the feed system. These results, along with the modeling approach, provide an important basis for the further study of in-machining monitoring and vibration controller design.

1. Introduction

The machining accuracy and efficiency of CNC machine tools largely depend on the performance of the feed system. Ball-screw feed systems are widely used in CNC machine tools due to its advantages. Its main functional components include a servo motor, a ball screw pair, and a carriage that moves with the nut along the axial direction. The dynamic characteristics of the ball screw system directly affect the dynamic behavior of the entire machine tool and considerably influence the machining quality of the tools. Therefore, with the increase in feed speed and the demand for high machining accuracy, the dynamic characteristics of feed systems have gradually become a trending research topic. Research results can provide theoretical bases for studying the kinematic accuracy of carriage and the vibration control of transmission systems.

In Refs. [1, 2], axial and torsional vibration models of the drive system were established on the basis of the theory of equal-section beams and finite elements; however, the studies did not consider bending vibration. In Ref. [3], the Ritz series method was adopted to represent the spatial dependence of the axial and torsional displacement fields of the screw shaft and compare the axial coupled torsional vibrations with the pure axial and torsional vibration modes. However, the bending and lateral vibrations of the screw shaft were not considered, and experimental verification was lacking. In Ref. [4], the power balance formula and the energy method were used to establish the mass, stiffness, and damping matrix expressions, in consideration of the coupling of axial and torsional vibration and bending vibration; however, the specific vibration equations were not given. In Ref. [5], the screw was simplified to the Timoshenko

beam in consideration of the coupling effect of bending and axial vibration. In addition, the nonlinear vibration characteristics of the ball screw system were studied by principal component analysis. However, the model in Ref. [5] only considered the screw shaft but not the entire system consisting of the ball screw, moving parts, nuts, support bearings, and a servo motor. In Refs. [6-8], lumped mass models for the entire system were developed. The lumped mass model can estimate the low-order axial and torsional modes of the feed system, but it cannot describe the flexible characteristics of the lead screw accurately. In Ref. [9], an axial dynamic model of a screw–workbench system was established, and the nonlinear characteristics of the axial vibration of the system were deduced and verified by power spectrum, phase trajectory, and correlation dimension. In Refs. [10, 11], a finite element model of the ball screw feed system was established, thus presenting the existence of the coupling terms with axial, torsional, and bending vibration in the system stiffness matrix. However, the model in Refs. [10, 11] is only suitable for specific systems. In Refs. [12-15], the dynamic characteristic of the ball screw feed system was analyzed by a hybrid model, where the flexibility of the screw shaft was considered. Okwudire et al. [16] improved the screw–nut interface model for high-performance ball screw feed drive system. The model can capture the coupling between axial and torsional vibration; moreover, a detailed screw–nut interface is proposed, implying that a considerable number of parameters must be known. Feng and Pan [17] used the lumped parameter method to analyze the influence of preload on the dynamic performance of a screw–nut system. In Refs. [18-21], the natural frequency and vibration mode of the beam with stepped eccentric distribution mass are calculated, and the free vibration and harmonic response analysis of multi-storey frame model with flexible foundation are studied on the basis of theory of single variable shear deformation and the Timoshenko beam and in consideration of the parabolic shear stress distribution on the beam section. Phung-Van et al. [22] used the Hamilton principle and higher-order shear deformation theory and derived the governing equations of the porous FG nanoplates. Loc et al. [23] proposed an effective formulation that combines the extended isogeometric approach and higher-order shear deformation theory to study the free vibration of cracked functionally graded material plates. In Refs. [24, 25], the axial vibration characteristics of flexible beams and the test method were introduced.

The present study focuses on analyzing the time-varying vibration characteristics of ball screw systems. First, the screw shaft is regarded as a continuous component for distribution parameter modeling, and the rest of the system (including the servo motor, the bearings at both ends, the carriage, and so on) are modeled as lumped masses. On the basis of Timoshenko beam theory and in consideration of its cross section and shearing effect, the Rayleigh-Ritz series method is used to construct the axial, torsional, transverse, and bending coupled vibration equations of the screw–carriage system. The influence of the carriage position and load on the vibration of the feed system is studied through numerical simulation, and the vibration response signals and vibration modes of the ball screw system at different carriage positions are given.

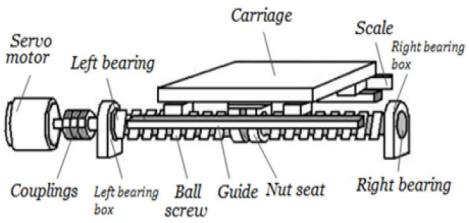

Fig. 1. Structure of a ball screw feed system.

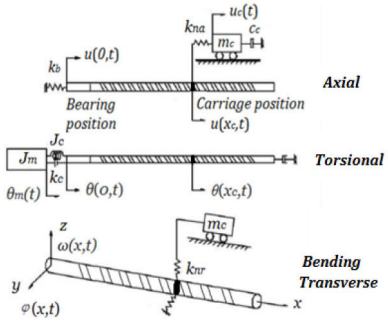

Fig. 2. Vibration model of a ball screw in all directions.

2. Coupled vibration model of ball screw systems

The structure of a ball screw feed system is shown in Fig. 1. The servo motor drives the lead screw rotating through the couplings, the lead screw is mounted on the frame through the support bearings at both ends, and the nut drives the carriage to move in the axial direction.

A model of the four vibration modes of the ball screw system is shown in Fig. 2. The screw shaft is considered a continuous system because of its flexibility, whereas the other elements are in lumped form. m_c represents the total mass of the carriage, and the carriage position x_c is the distance from the left bearing support end to the center of the carriage. The screw shaft is a continuous body, and its distribution parameters include density ρ, diameter d, length l, moment of inertia of the ball screw J, moment of inertia of the cross section of the screw shaft around the x-axis I_x, Young's modulus E, shear modulus G, and lead s. The lumped parameters include the axial stiffness of the bearing k_b, torsional stiffness of the coupling k_c, axial stiffness of the nut k_{na}, moment of inertia of the motor J_m, moment of inertia of the coupling J_c, and radial support stiffness of the nut k_{nr}. The guide rail is considered a rigid body in this hybrid model.

2.1 Axial and torsional vibration models

The axial and torsional vibrations of the screw are represented by the axial displacement function u (x, t) and the tor-

sional displacement function $\theta(x, t)$, respectively. $u_c(t)$ represents the displacement of the carriage, and $\theta_m(t)$ represents the angular displacement of the motor.

The total kinetic energy T_{at}, of the coupled axial and torsional vibration of the screw system, including the kinetic energy of the lead screw, carriage, motor, and coupling, is

$$T_{at}=\frac{1}{2}m_c\dot{u}_c^2(t)+\frac{1}{2}J_m\dot{\theta}_m^2(t)+\frac{1}{2}J_c\left(\frac{1}{2}\left(\dot{\theta}_m(t)+\dot{\theta}(0,t)\right)\right)^2+\frac{1}{2}\rho I_x\int_0^l\dot{\theta}(x,t)^2dx+\frac{1}{2}\rho A\int_0^l\dot{u}(x,t)^2dx. \tag{1}$$

The symbol (.) represents the derivative to t. The potential energy of the coupled axial and torsion vibration of the screw system, including axial and torsional strain energy U_{at}, is

$$U_{at}=\frac{1}{2}EA\int_0^l u'(x,t)^2dx+\frac{1}{2}GI_x\int_0^l\theta'(x,t)^2dx+\frac{1}{2}k_bu(0,t)^2+\frac{1}{2}k_{na}\delta_{na}^2+\frac{1}{2}k\left[\theta_m(t)-\theta(0,t)\right]_c^2 \tag{2}$$

where the symbol (') represents the derivative to x. The x-direction displacement δ_{na} of the screw nut joint surface can be expressed as

$$\delta_{na}=u_c(t)-\left[u(x_c,t)+\theta(x_c,t)\frac{s}{2\pi}\right] \tag{3}$$

and the external force potential energy W_{at}, obtained by the volume force transformed by inertial force can be expressed as

$$W_{at}=\int_0^l\rho Au(x,t)\ddot{u}(x,t)dx+\int_0^l\rho I_x\theta(x,t)\ddot{\theta}(x,t)dx\,. \tag{4}$$

Energy dissipation R_{at} can be expressed as

$$R_{at}=\frac{1}{2}\eta GI_x\int_0^l\left(\dot{\theta}(x,t)'\right)^2dx+\frac{1}{2}\eta EA\int_0^L\left(\dot{u}(x,t)'\right)^2dx+\frac{1}{2}c_c\left(\dot{\theta}(0,t)-\dot{\theta}_m(t)\right)^2+\frac{1}{2}c_n\left(\dot{u}_c(t)-\dot{u}(x_c,t)-s\dot{\theta}(x_c,t)\right)^2+\frac{1}{2}c_b\dot{u}(0,t)^2 \tag{5}$$

with the damping loss factor η of the structure.

On the basis of the Rayleigh–Ritz method, the displacement component can be selected as follows:

$$\begin{cases}u(x,t)=u_0+\sum_{i=1}^{N_u}u_i(x)q_{ui}(t)=u_0+\mathbf{u}(x)^T\mathbf{q}_\mathbf{u}(t)\\ \theta(x,t)=\theta_0+\sum_{i=1}^{N_\theta}\theta_i(x)q_{\theta i}(t)=\theta_0+\boldsymbol{\theta}(x)^T\mathbf{q}_\boldsymbol{\theta}(t)\end{cases} \tag{6}$$

where u_0, θ_0 are initial positions; $\mathbf{u}(x)\in\mathbb{R}^{N_u}$, $\boldsymbol{\theta}(x)\in\mathbb{R}^{N_\theta}$ are basis function vectors that satisfy the displacement boundary condition; $\mathbf{q}_\mathbf{u}(t)\in\mathbb{R}^{N_u}$, $\mathbf{q}_\boldsymbol{\theta}(t)\in\mathbb{R}^{N_\theta}$ are unrelated time functions and corresponding generalized coordinates. Then, Eq. (6) is taken into Eqs. (1)-(5); under the assumption $u_0 = \theta_0 = 0$, the following finite approximation is obtained:

$$\begin{aligned}T_{at}=&\frac{1}{2}m_c\dot{u}_c^2(t)+\frac{1}{2}J_m\dot{\theta}_m^2(t)+\frac{1}{2}\frac{J_c}{4}\left(\dot{\theta}_m^2(t)+2\dot{\theta}_m\boldsymbol{\theta}(0)^T\dot{\mathbf{q}}_\boldsymbol{\theta}(t)+\boldsymbol{\theta}(0)^T\dot{\mathbf{q}}_\boldsymbol{\theta}(t)\boldsymbol{\theta}(0)\mathbf{q}_\boldsymbol{\theta}^T(t)\right)\\&+\frac{1}{2}\rho I_x\dot{\mathbf{q}}_\boldsymbol{\theta}^T(t)\mathbf{q}_\boldsymbol{\theta}(t)\int_0^l\boldsymbol{\theta}(x)^T\boldsymbol{\theta}(x)dx+\\&\frac{1}{2}\rho A\dot{\mathbf{q}}_\mathbf{u}^T(t)\dot{\mathbf{q}}_\mathbf{u}(t)\int_0^l\mathbf{u}(x)^T\mathbf{u}(x)dx\end{aligned} \tag{7}$$

The total potential energy Π_{at} is

$$\begin{aligned}\Pi_{at}=U_{at}-W_{at}=&\frac{1}{2}EA\mathbf{q}_\mathbf{u}^T(t)\mathbf{q}_\mathbf{u}(t)\int_0^l\mathbf{u}'(x)\mathbf{u}'(x)^Tdx+\\&\frac{1}{2}GI_X\mathbf{q}_\boldsymbol{\theta}^T(t)\mathbf{q}_\boldsymbol{\theta}(t)\int_0^l\boldsymbol{\theta}'(x)\boldsymbol{\theta}'(x)^Tdx+\frac{1}{2}k_b\mathbf{u}(0)\mathbf{q}_\mathbf{u}^T(t)\mathbf{u}(0)^T\mathbf{q}_\mathbf{u}(t)\\&+\frac{1}{2}k_{na}\left[u_c-\mathbf{u}(x_c)^T\mathbf{q}_\mathbf{u}(t)-\boldsymbol{\theta}(x_c)\frac{s}{2\pi}\mathbf{q}_\boldsymbol{\theta}(t)\right]^2+\frac{1}{2}k_c\\&\left[\theta_m(t)-\boldsymbol{\theta}(0)^T\mathbf{q}_\boldsymbol{\theta}(t)\right]^2-\mathbf{q}_\mathbf{u}(t)\ddot{\mathbf{q}}_\mathbf{u}(t)\int_0^l\rho A\mathbf{u}(x)^T\mathbf{u}(x)dx\\&+\mathbf{q}_\boldsymbol{\theta}(t)\ddot{\mathbf{q}}_\boldsymbol{\theta}(t)\int_0^l\rho I_x\boldsymbol{\theta}(x)^T\boldsymbol{\theta}(x)dx\,.\end{aligned} \tag{8}$$

The energy dissipation R_{at} is

$$\begin{aligned}R_{at}=&\frac{1}{2}\eta GI_x\dot{\mathbf{q}}_\boldsymbol{\theta}^T(t)\int_0^l\boldsymbol{\theta}'(x)\boldsymbol{\theta}'(x)^Tdx\dot{\mathbf{q}}_\boldsymbol{\theta}(t)+\frac{1}{2}\eta EA\dot{\mathbf{q}}_\mathbf{u}^T(t)\\&\int_0^l\mathbf{u}'(x)\mathbf{u}'(x)^Tdx\dot{\mathbf{q}}_\mathbf{u}(t)+\frac{1}{2}c_c\left[\boldsymbol{\theta}^T(0)\dot{\mathbf{q}}_\boldsymbol{\theta}(t)-\dot{\theta}_m\right]^2\\&+\frac{1}{2}c_n\left[\dot{u}_c-\mathbf{u}^T(x_c)\dot{\mathbf{q}}_\mathbf{u}(t)-s\boldsymbol{\theta}(x_c)\dot{\mathbf{q}}_\boldsymbol{\theta}(t)\right]^2\\&+\frac{1}{2}c_b\dot{\mathbf{q}}_\mathbf{u}^T(t)\mathbf{u}(0)\mathbf{u}(0)^T\dot{\mathbf{q}}_\mathbf{u}(t)\,.\end{aligned} \tag{9}$$

2.2 Bending and transverse vibration models

The bending and transverse vibration of the screw are represented by a bending displacement function $\varphi(x, t)$ and a transverse displacement function $\omega(x, t)$, respectively. $\omega_c(t)$ represents the vertical translation displacement of the ball screw system, and $\theta_c(t)$ represents the rotation displacement of the ball screw. In accordance with Timoshenko beam theory, the axial displacement caused by transverse vibration is ignored, and the total transverse deformation $\omega_z(x, t)$ is defined as the displacement along the z direction, including transverse deformation $\omega(x, t)$ and bending deformation $\omega_b(x, t)$.

$$\begin{cases}\omega_z(x,t)=\omega(x,t)+\omega_b(x,t)\\ \omega_b(x,t)=\int_0^l\varphi(x,t)dx.\end{cases} \tag{10}$$

The total kinetic energy T_{hw} of the bending and transverse vibration of the lead screw, including the kinetic energy of the transverse vibration and the rotation of the lead screw, is

$$T_{hw}=\frac{1}{2}m_c\dot{\omega}_c^2(t)+\frac{1}{2}J\dot{\theta}_c^2(t)+\frac{1}{2}\int_0^l\rho A\dot{\omega}(x,t)^2dx+\frac{1}{2}\int_0^l\rho I_y\dot{\varphi}(x,t)^2dx \quad (11)$$

Given bending and shear deformation and the limitation of the radial stiffness of the nut, Eq. (10) is taken into the strain potential energy U_{hw}, which is represented as follows:

$$U_{hw}=\frac{1}{2}\int_0^l EI_y\left(\varphi'(x,t)\right)^2dx+\frac{1}{2}\int_0^l\kappa GA\left(\omega'(x,t)-\varphi(x,t)\right)^2dx+\frac{1}{2}k_{nr}\left(\omega(x,t)+\int_0^l\varphi(x,t)dx\right)^2+\frac{1}{2}k_{nt}\delta_{nt}^2+\frac{1}{2}k_{br}\omega(0,t)^2+\frac{1}{2}k_{n\omega}\left(\omega_c(t)+\omega(x_c,t)\right)^2+\frac{1}{2}k_{n\varphi}\theta_c(t)^2 \quad (12)$$

With the shear coefficient κ of the section, the moment of inertia I_y of the cross section of the screw shaft around the *y*-axis, the torsional stiffness k_{nt} of the screw–nut interface, the radial stiffness k_{br} of the bearing, the vertical stiffness $k_{n\omega}$ of the slider, and the rotate stiffness $k_{n\varphi}$ of the slider. In Eq. (12),

$$\delta_{nt}=\theta_c(t)-\theta(x_c,t). \quad (13)$$

The external force potential energy W_{hw} obtained by the volume force transformed by the inertial force is expressed as

$$W_{hw}=\int_0^l\rho A\omega(x)\ddot{\omega}(x,t)dx+\int_0^l\rho I_y\varphi(x)\ddot{\varphi}(x,t)dx. \quad (14)$$

The energy dissipation R_{hw} is

$$R_{hw}=\frac{1}{2}c_{n\omega}\dot{\omega}_c^2(t)+\frac{1}{2}c_{n\varphi}\dot{\theta}_c^2(t)+\frac{1}{2}\eta\kappa GA\int_0^l\left(\dot{\omega}'(x,t)-\dot{\varphi}(x,t)\right)^2dx+\frac{1}{2}\eta EI_y\int_0^l\dot{\varphi}(x,t)^2dx+\frac{1}{2}c_{br}\dot{\omega}(0,t)^2+\frac{1}{2}c_{n\omega}\dot{\omega}(x_c,t)^2 \quad (15)$$

With the radial damping coefficient c_{br} of the bearings at both ends and the rotational damping coefficient $c_{n\omega}$, $c_{n\varphi}$ of bearings around the *y* and *z* axes.

On the basis of the Rayleigh–Ritz method, the displacement component can be selected as follows:

$$\begin{cases}\omega(x,t)=\omega_0+\sum_{i=1}^{N_\omega}\omega_i(x)q_{\omega i}(t)=\omega_0+\boldsymbol{\omega}(x)^T\mathbf{q}_\omega(t)\\ \varphi(x,t)=\varphi_0+\sum_{i=1}^{N_\varphi}\varphi_i(x)q_{\varphi i}(t)=\varphi_0+\boldsymbol{\varphi}(x)^T\mathbf{q}_\varphi(t)\end{cases} \quad (16)$$

where ω_0, φ_0 are initial positions; $\boldsymbol{\omega}(x)\in\mathbb{R}^{N\omega}$, $\boldsymbol{\varphi}(x)\in\mathbb{R}^{N_\varphi}$ are basis function vectors that satisfy the displacement boundary condition; $\mathbf{q}_\omega(t)\in\mathbb{R}^{N_\omega}$, $\mathbf{q}_\varphi(t)\in\mathbb{R}^{N_\varphi}$ are unrelated time functions and corresponding generalized coordinates. By combining $u_c(t),\theta_m(t),\omega_c(t),\theta_c(t),\mathbf{q}_\mathbf{u}(t)$ *and* $\mathbf{q}_\boldsymbol{\theta}(t)$, the generalized coordinates of the ball screw coupling vibration system in a vector is defined as

$$\Delta=\left[u_c(t)\theta_m(t)\omega_c(t)\theta_c(t)\mathbf{q}_\mathbf{u}(t)^T\mathbf{q}_\boldsymbol{\theta}(t)^T\mathbf{q}_\varphi(t)^T\mathbf{q}_\omega(t)^T\right]^T\in\mathbb{R}^{N_u+N_\theta+N_\omega+N_\varphi+4}. \quad (17)$$

Then, Eq. (14) is taken into Eqs. (11)-(13); under the assumption $\omega_0 = \varphi_0 = 0$, the following finite approximation is obtained:

$$T_{hw}=\frac{1}{2}m_c\dot{\omega}_c^2(t)+\frac{1}{2}J\dot{\theta}_c^2(t)+\frac{1}{2}\rho A\dot{\mathbf{q}}_\omega^T(t)\dot{\mathbf{q}}_\omega(t)\int_0^l\boldsymbol{\omega}(x)^T\boldsymbol{\omega}(x)dx+\frac{1}{2}\rho I_y\dot{\mathbf{q}}_\varphi^T(t)\dot{\mathbf{q}}_\varphi(t)\int_0^l\boldsymbol{\varphi}(x)^T\boldsymbol{\varphi}(x)dx \quad (18)$$

The total potential energy Π_{hw} is

$$\Pi_{hw}=U_{hw}-W_{hw}=\frac{1}{2}EI_y\mathbf{q}_\varphi^T(t)\mathbf{q}_\varphi(t)\int_0^l\boldsymbol{\varphi}'(x)\boldsymbol{\varphi}'(x)^Tdx+\frac{1}{2}\kappa GA\int_0^L\left[\boldsymbol{\omega}'(x)^T\mathbf{q}_\omega(t)\boldsymbol{\varphi}(x)^T\mathbf{q}_\varphi(t)\right]^2dx+\frac{1}{2}k_{nt}\left(\theta_c(t)-\boldsymbol{\theta}(x)\mathbf{q}_\boldsymbol{\theta}(t)\right)^2+\frac{1}{2}k_{br}\boldsymbol{\omega}(0)^T\mathbf{q}_\omega(t)\boldsymbol{\omega}(0)\mathbf{q}_\omega^T(t)+\frac{1}{2}k_{n\omega}\left(\omega_c(t)+\boldsymbol{\omega}(x_c)^T\mathbf{q}_\omega(t)\right)^2+\frac{1}{2}k_{n\varphi}\theta_c^2(t)+\frac{1}{2}k_{nr}\left[\boldsymbol{\omega}(x)^T\mathbf{q}_\omega(t)+\int_0^l\boldsymbol{\varphi}(x_c)\mathbf{q}_\varphi(t)dx\right]^2-\mathbf{q}_\omega(t)\ddot{\mathbf{q}}_\omega(t)\int_0^l\rho A\boldsymbol{\omega}(x)^T\boldsymbol{\omega}(x)dx-\mathbf{q}_\varphi(t)\ddot{\mathbf{q}}_\varphi(t)\int_0^l\rho I_y\boldsymbol{\varphi}(x)^T\boldsymbol{\varphi}(x)dx \quad (19)$$

The energy dissipation R_{hw} is

$$R_{hw}=\frac{1}{2}c_{n\omega}\dot{\omega}_c^2(t)+\frac{1}{2}c_{n\varphi}\dot{\theta}_c^2(t)+\frac{1}{2}\eta\kappa GA\int_0^l\left(\boldsymbol{\omega}'(x)^T\dot{\mathbf{q}}_\omega(t)-\boldsymbol{\varphi}(x)^T\dot{\mathbf{q}}_\varphi(t)\right)^2dx+\frac{1}{2}\eta EI_y\int_0^l\dot{\mathbf{q}}_\varphi(t)^T\boldsymbol{\varphi}(x)\boldsymbol{\varphi}(x)^T\dot{\mathbf{q}}_\varphi(t)dx+\frac{1}{2}c_{br}\dot{\mathbf{q}}_\omega(t)^T\boldsymbol{\omega}(0)\boldsymbol{\omega}(0)^T\dot{\mathbf{q}}_\omega(t)+\frac{1}{2}c_{n\omega}\mathbf{q}_\omega(t)^T\boldsymbol{\omega}(x_c)\boldsymbol{\omega}(x_c)^T\dot{\mathbf{q}}_\omega(t) \quad (20)$$

The mass matrix **M** of the coupling vibration can be expressed as

$$\mathbf{M}=\begin{vmatrix} m_c & 0 & 0 & 0 & 0 & 0 & 0 & 0\\ 0 & J_m+\frac{1}{4}J_c & 0 & 0 & 0 & \frac{1}{4}J_c\boldsymbol{X}^T & 0 & 0\\ 0 & 0 & m_c & 0 & 0 & 0 & 0 & 0\\ 0 & 0 & 0 & J & 0 & 0 & 0 & 0\\ 0 & 0 & 0 & 0 & rA\boldsymbol{A} & 0 & 0 & 0\\ 0 & \frac{1}{4}J_c\boldsymbol{X} & 0 & 0 & 0 & rI_x\boldsymbol{B}+\frac{1}{4}J_c\boldsymbol{L} & 0 & 0\\ 0 & 0 & 0 & 0 & 0 & 0 & rA\boldsymbol{D} & 0\\ 0 & 0 & 0 & 0 & 0 & 0 & 0 & rI_y\boldsymbol{C}\end{vmatrix}. \quad (21)$$

The stiffness matrix **K** of the coupling vibration can be expressed as

$$\mathbf{K}=\begin{vmatrix} k_{na} & 0 & 0 & 0 & -k_{na}\boldsymbol{Z}^T\frac{s}{2\pi} & -k_{na}\boldsymbol{Y} & 0 & 0 \\ 0 & k_c & 0 & 0 & -k_c\boldsymbol{X}^T & 0 & 0 & 0 \\ 0 & 0 & k_{n\omega} & 0 & 0 & 0 & 0 & k_{n\omega}\boldsymbol{D}^T \\ 0 & 0 & 0 & k_{nt}+k_{nj} & 0 & k_{nt}\boldsymbol{\theta}(x)^T & 0 & 0 \\ -k_{na}\boldsymbol{Z}\frac{s}{2\pi} & -k_c\boldsymbol{X} & 0 & 0 & \bar{A} & k_{na}\boldsymbol{YZ}\frac{s}{2\pi} & 0 & 0 \\ -k_{na}\boldsymbol{Y}^T & 0 & 0 & k_{nt}\boldsymbol{\theta}(x) & k_{na}\boldsymbol{Y}^T\boldsymbol{Z}\frac{s}{2\pi} & \bar{B} & 0 & 0 \\ 0 & 0 & 0 & 0 & 0 & 0 & \bar{C} & \bar{L}\boldsymbol{O}^T\boldsymbol{Q} \\ 0 & 0 & k_{n\omega}\boldsymbol{D} & 0 & 0 & 0 & \bar{L}\boldsymbol{O}\boldsymbol{Q} & \bar{D} \end{vmatrix}. \tag{22}$$

The damping matrix **C** of the coupling vibration can be expressed as

$$\mathbf{C}=\begin{vmatrix} c_n & 0 & 0 & 0 & -c_n s\boldsymbol{Z}^T & c_n\boldsymbol{Y}^T & 0 & 0 \\ 0 & c_c & 0 & 0 & c_c\boldsymbol{X}^T & 0 & 0 & 0 \\ 0 & 0 & c_{n\omega} & 0 & 0 & 0 & 0 & 0 \\ 0 & 0 & 0 & c_{n\varphi} & 0 & 0 & 0 & 0 \\ -c_n s\boldsymbol{Z} & c_c\boldsymbol{X} & 0 & 0 & \bar{E} & c_n s\boldsymbol{Y}\boldsymbol{Z}^T & 0 & 0 \\ c_n\boldsymbol{Y} & 0 & 0 & 0 & c_n s\boldsymbol{Y}^T\boldsymbol{Z} & \bar{F} & 0 & 0 \\ 0 & 0 & 0 & 0 & 0 & 0 & \bar{G} & -\eta\kappa GA\boldsymbol{U} \\ 0 & 0 & 0 & 0 & 0 & 0 & -\eta\kappa GA\boldsymbol{U} & \bar{H} \end{vmatrix} \tag{23}$$

where

$$\begin{aligned}
&\boldsymbol{A}=\int_0^l \mathbf{u}(x)^T\mathbf{u}(x)dx,\quad \boldsymbol{B}=\int_0^l \boldsymbol{\theta}(x)^T\boldsymbol{\theta}(x)dx\\
&\boldsymbol{C}=\int_0^l \boldsymbol{\varphi}(x)^T\boldsymbol{\varphi}(x)dx,\quad \boldsymbol{D}=\boldsymbol{\omega}(x_c)^T\\
&\boldsymbol{E}=\int_0^l \mathbf{u}'(x)^T\mathbf{u}(x)dx,\quad \boldsymbol{F}=\int_0^l \mathbf{q}'(x)^T\mathbf{q}(x)dx\\
&\boldsymbol{G}=\int_0^l \boldsymbol{\varphi}'(x)^T\boldsymbol{\varphi}(x)dx,\quad \boldsymbol{H}=\int_0^l \boldsymbol{\omega}'(x)^T\boldsymbol{\omega}(x)dx\\
&\boldsymbol{L}=\boldsymbol{\theta}(0)^T\boldsymbol{\theta}(0),\boldsymbol{N}=\mathbf{u}(x_c)^T\mathbf{u}(x_c),\boldsymbol{O}=\boldsymbol{\omega}(x)\\
&\boldsymbol{P}=\boldsymbol{\omega}(x)^T\boldsymbol{\omega}(x),\boldsymbol{Q}=\int_0^l \boldsymbol{\varphi}(x)dx,\boldsymbol{R}=\boldsymbol{\theta}(x_c)^T\boldsymbol{\theta}(x_c)\\
&\boldsymbol{S}=\boldsymbol{\omega}(0)^T\boldsymbol{\omega}(0),\boldsymbol{T}=\boldsymbol{\varphi}(x)^T\boldsymbol{\varphi}(x),\boldsymbol{U}=\int_0^l \boldsymbol{\omega}'(x)\boldsymbol{\varphi}(x)^T dx,\\
&\boldsymbol{V}=\mathbf{u}(0)^T\mathbf{u}(0),\boldsymbol{W}=\boldsymbol{\omega}(x_c)^T\boldsymbol{\omega}(x_c),\\
&\boldsymbol{X}=\boldsymbol{\theta}(0),\ \boldsymbol{Y}=\mathbf{u}(x_c),\ \boldsymbol{Z}=\boldsymbol{\theta}(x_c)\\
&\bar{A}=GI_x\boldsymbol{F}+2rJ\boldsymbol{B}+k_c\boldsymbol{L}+k_{na}\left(\frac{s}{2\pi}\right)^2\boldsymbol{R},\\
&\bar{B}=EA\boldsymbol{E}+k_b\boldsymbol{V}+k_{na}\boldsymbol{N}-2rA\boldsymbol{A}+k_{nt}\boldsymbol{\theta}^2(x),\\
&\bar{C}=EI_y\boldsymbol{G}+\kappa GA\boldsymbol{C}+k_{nr}\boldsymbol{Q}^2,\\
&\bar{D}=\kappa GA\boldsymbol{H}+k_{nr}\boldsymbol{P}+k_{br}\boldsymbol{S}+k_{n\omega}\boldsymbol{W},\\
&\bar{E}=\eta GI_x\boldsymbol{F}+c_c\boldsymbol{L}+c_n s^2\boldsymbol{R},\\
&\bar{F}=\eta EA\boldsymbol{E}+c_n\boldsymbol{N}+c_b\boldsymbol{V},\\
&\bar{G}=(\eta EI_Y+\eta\kappa GA)\boldsymbol{C},\\
&\bar{H}=c_{br}\boldsymbol{S}+c_{n\omega}\boldsymbol{W}+\eta\kappa GA\boldsymbol{H},\\
&\bar{L}=(k_{nr}-\kappa GA)
\end{aligned} \tag{24}$$

2.3 Modal analysis

The equation of motion of the system can be expressed as

$$[\mathbf{M}]\ddot{\mathbf{q}}+[\mathbf{C}]\dot{\mathbf{q}}+[\mathbf{K}]\mathbf{q}=\mathbf{F}_\mathbf{f}. \tag{25}$$

$\mathbf{F_f}$ represents the generalized force matrix. In Ritz series modeling, the use of the basis function, which is similar to the actual vibration mode of the system, is an important means to improve the convergence rate and accuracy of the system modal. In this study, the basic function vectors **u**(*x*) and **θ**(*x*) required for the axial and torsional modes of the system are defined in accordance with the mode shapes obtained by simulation, and the method is defined as the Ritz series method based on the hybrid basis functions. **u**(*x*) and **θ**(*x*) must meet two conditions:

a) The vector is linearly independent, and the vector elements are continuous functions.

b) The physical boundary conditions of a ball screw drive system are met.

The basis function shown in Eq. (26) is defined and formed into a two-dimensional axial mode basis function vector **u**(*x*).

$$\begin{aligned} u_1(x)&=1, && for\quad x\in[0,l]\\ u_2(x)&=\begin{cases}\dfrac{x}{x_c}, & for\quad x\in[0,x_c]\\ 1, & for\quad x\in[x_c,l]\end{cases}\end{aligned} \tag{26}$$

The maximum deformation of the torsional vibration mode exists at both ends of the lead screw, and the deformation at the worktable position is relatively small; thus, the cosine function shown in Eq. (27) can be used to form the N_θ dimensional torsional vibration mode basis function vector **θ**(*x*).

$$\theta_i(x)=\cos\left((i-1)\pi\frac{x}{l}\right),\qquad i=1,2,...,N_\theta \tag{27}$$

The maximum deformation of the transverse and bending vibration mode exists in the middle of the lead screw, and the deformation at the both ends is relatively small; thus, the sine function shown in Eq. (28) can be used to form the $N_{\omega/\varphi}$ dimensional transverse and bending vibration mode basis function vectors **ω**(*x*) and **φ**(*x*) .

$$\omega_i(x)=\varphi_i(x)=\sin\left((i-1)\pi\frac{x}{l}\right),\qquad i=1,2,...,N_{\omega/\varphi} \tag{28}$$

By solving the characteristic equation of undamped systems,

$$\left[\mathbf{K}-\omega_i^2\mathbf{M}\right]\boldsymbol{\upsilon}_\mathbf{i}=0 \tag{29}$$

where the resonance frequencies ω_i as eigenvalues and the modal shapes as eigenvectors $\boldsymbol{\upsilon}_\mathbf{i}$. The eigenvector of the *i* order is

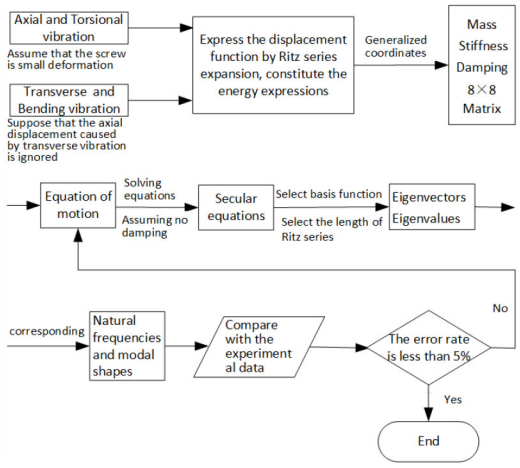

Fig. 3. Flowchart of the entire research process.

$$\begin{aligned}&\boldsymbol{\upsilon}_{\mathrm{i}}=\left[\boldsymbol{\upsilon}_{\mathrm{u_c}}\ \boldsymbol{\upsilon}_{\theta_{\mathrm{m}}}\ \boldsymbol{\upsilon}_{\omega_{\mathrm{c}}}\ \boldsymbol{\upsilon}_{\theta_{\mathrm{c}}}\ \boldsymbol{\upsilon}_{\mathrm{u}}\ \boldsymbol{\upsilon}_{\theta}\ \boldsymbol{\upsilon}_{\omega}\ \boldsymbol{\upsilon}_{\varphi}\right]^{T},\\&\boldsymbol{\upsilon}_{\mathrm{u}}\in\mathbb{R}^{N_u},\boldsymbol{\upsilon}_{\theta}\in\mathbb{R}^{N_\theta},\boldsymbol{\upsilon}_{\omega}\in\mathbb{R}^{N_\omega},\boldsymbol{\upsilon}_{\varphi}\in\mathbb{R}^{N_\varphi}\end{aligned}. \tag{30}$$

The axial, torsional, transverse, and bending vibration components of the *i* order modal function are as follows:

$$\begin{aligned}&\boldsymbol{\Psi}_{\mathrm{u_i}}(x)=\mathbf{u}(x)\boldsymbol{\upsilon}_{\mathrm{u}}^{T},\ \ \boldsymbol{\Psi}_{\theta_{\mathrm{i}}}(x)=\boldsymbol{\theta}(x)\boldsymbol{\upsilon}_{\theta}^{T}\\&\boldsymbol{\Psi}_{\omega_{\mathrm{i}}}(x)=\boldsymbol{\omega}(x)\boldsymbol{\upsilon}_{\omega}^{T},\ \ \boldsymbol{\Psi}_{\varphi_{\mathrm{i}}}(x)=\boldsymbol{\varphi}(x)\boldsymbol{\upsilon}_{\varphi}^{T}\end{aligned}. \tag{31}$$

Next, numerical simulation analysis is conducted. The results are compared with the experimental data to verify the correctness of the theoretical analysis. Fig. 3 shows the flowchart of the entire research process.

3. Experimental verification

The test rig of the ball screw feed system is shown in Fig. 4. Fig. 5 shows the structure and size of the ball screw used in the test rig. The detailed parameters are shown in Table 1. To verify the influence on the vibration at different positions of the carriage, the vibration frequencies and modes at three different positions were tested. The screw length *l* is defined as the distance between the fixed bearing support at both ends; thus, the point $x = 0$ is at the motor end, and another point $x = l$ is at the end, which is far away from the motor. The three positions of the carriage are 0.25 *l*, 0.5 *l*, and 0.8 *l*, respectively.

As shown in Fig. 4, a hammer was used for excitation, and the vibration response signals were collected by a three-axis accelerometer and laser sensor. Axial vibration is obtained by exerting an excitation to the carriage along the direction of motion and measuring it using the laser sensor mounted at the end of the lead screw. Transverse vibration is obtained by motion excitation at different carriage speeds and measured by the acceleration sensors mounted on the carriage. Bending vibration is obtained by excitation at different positions on the carriage and measured by picking up the signals of the meas-

Table 1. Parameter values used in the model.

Name	Value	Unit	Physical significance
ρ	7.85×10^{3}	kg/m^3	Density of the ball screw shaft
d	0.036	m	Diameter of the ball screw shaft
l	1.310	m	Length of the ball screw shaft
s	0.01	m	Lead of the ball screw shaft
G	$8*10^{10}$	N/m^2	Shear modulus
E	$2.05*10^{11}$	N/m^2	Young's modulus
I_x	1.65×10^{-8}	m^4	Moment of inertia of the cross section of the screw shaft around the *x*-axis
I_y	8.24×10^{-8}	m^4	Moment of inertia of the cross section of the screw shaft around the *y*-axis
J	0.048	kg.m^2	Moment of inertia of the ball screw
J_m	30×10^{-4}	kg.m^2	Moment of inertia of the motor
J_c	$2.003*10^{-4}$	kg.m^2	Moment of inertia of the coupling
k_{na}	9×10^{7}	N/m	Axial stiffness of the nut
k_{nr}	5.6×10^{7}	N/m	Radial support stiffness of the nut
k_b	8.5×10^{8}	N/m	Axial stiffness of the bearing
k_c	4.2×10^{3}	N.m/rad	Torsional stiffness of the coupling
η	1×10^{-4}	s	Factor of damping coefficient proportional to the stiffness
A	1.018×10^{-3}	m^2	Cross-section area of the ball screw shaft
m_c	345	kg	Weight of the table

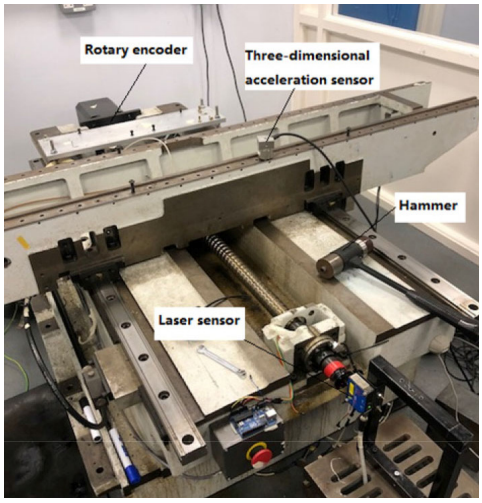

Fig. 4. Test rig of the ball screw feed.

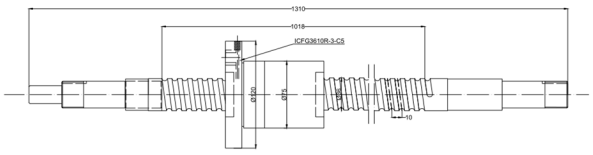

Fig. 5. Structure and size of the ball screw used in the test rig.

Table 2. Comparison of the first five natural frequencies between simulation and measurement.

Order	Natural frequency (simulated) (Hz)			
	x_c = 0.25l	x_c = 0.5l	x_c = 0.8l	x_c = 1l
1	33.8	31.0	29.8	29.2
2	195.0	185.8	190.2	192.7
3	293.5	313.3	337.5	350.9
4	466.8	459.6	462.9	470.5
5	1151.6	1139.7	1147.2	1170.0
Order	Natural frequency (measured) (Hz)			
	x_c = 0.25l	x_c = 0.5l	x_c = 0.8l	x_c = 1l
1	35	32	31	30
2	197	188	191	192
3	294	315	335	348
4	470	463	466	472
5	1150	1142	1145	1168

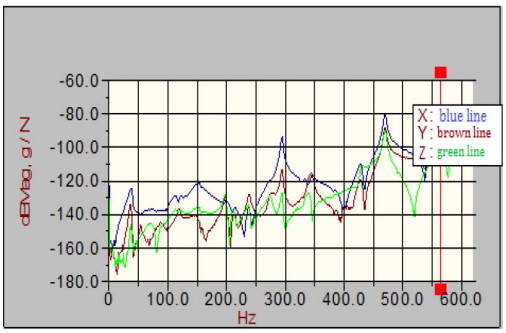

Fig. 6. Three-direction frequency response at carriage.

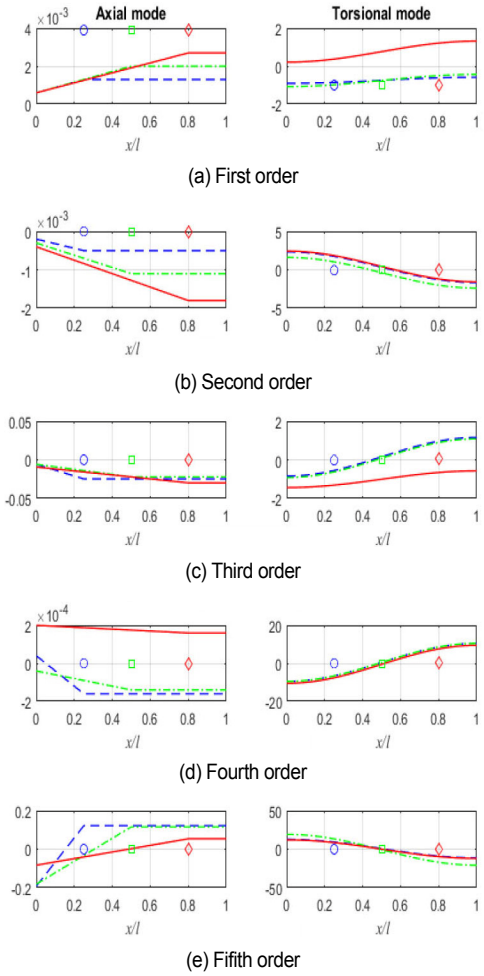

Fig. 7. Axial and torsional mode shapes at different carriage positions (plots in the left column are the axial components, and those on the right are the torsional components, --○: x = 0.25 l; —·—□: x = 0.5 l; — ◇: x = 0.8 l).

uring points distributed on the lead screw. The experimental anti-aliasing filter frequency is set to 400 Hz, the response sampling frequency is 1500 Hz, the sampling frequency of the pulse is 6000 Hz, and the time-varying multiple is 4. Fig. 6 shows the frequency response curve in x, y, z directions. as measured by the three-way acceleration sensor at x = 0.5 l. The abscissa is the frequency, and the ordinate represents the logarithmic amplitude in dB form. Table 2 shows the results of the first five natural frequencies obtained by simulation and measurement at different carriage positions.

During the machining of the workpieces, the position of the carriage constantly changes, resulting in changes in the vibration characteristics of the system. Fig. 7 shows the axial and torsional mode shapes of the ball screw at different carriage positions. The first-order modes of the screw shaft are presented in Fig. 7(a). The first-order vibration of the ball screw is mainly the axial vibration of the lead screw and greatly affected by the carriage position. The axial mode displacement of the lead screw increases from the left support bearing end to the carriage, and almost no deformation occurs from the carriage to the right support bearing end; this result is similar to the spring-mass system. However, as the carriage moves away from the motor, the torsional deformation of the lead screw rises slightly, resulting in the slight increase in the torsional vibration amplitude of the carriage. Fig. 7(b) represents the second-order mode of the ball screw. The second-order vibration is mainly the torsional vibration of the lead screw. With the changing direction and small axial vibration, the torsion angle increases at both ends of the support bearings. Fig. 7(c) represents the third-order vibration of the ball screw system. The third-order vibration is represented by the coupled axial and torsional vibration of the lead screw. Fig. 7(d) represents the fourth-order vibration of the ball screw system. The fourth-order vibration is represented by slight axial vibration; however, torsional vibration plays the major role. Fig. 7(e) represents the fifth-order vibration mode of the ball screw system. The fifth-order vibration is represented by the strong coupled axial and torsional vibration of the lead screw.

Fig. 8 shows the first three modes of the transverse and bending vibration of the ball screw system. The first-order modes of the screw shaft are presented in Fig. 8(a). The bending vibration of the ball screw is independent of the position of the carriage; however, transverse vibration is mainly affected

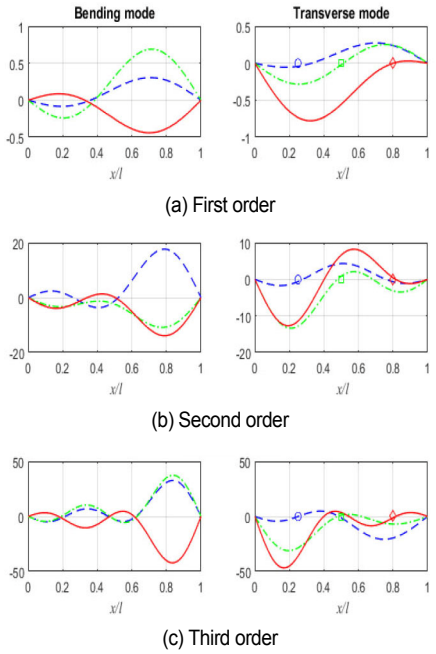

(a) First order

(b) Second order

(c) Third order

Fig. 8. Bending and transverse mode shapes at different carriage positions (left pictures depict the bending component, and right pictures depict the transverse component, - - ○: x = 0.25 *l*; —·—□: x = 0.5 *l*; — ◇: x = 0.8 *l*).

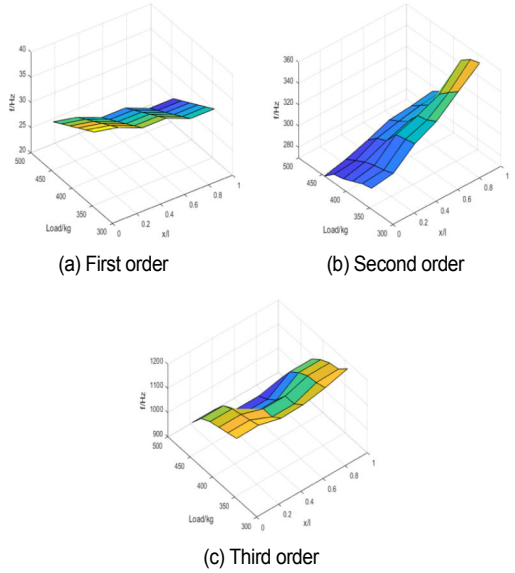

(a) First order

(b) Second order

(c) Third order

Fig. 9. Frequencies of axial and torsional vibrations at different carriage positions and loads.

by carriage position, the transverse mode displacement of the lead screw increases and decreases from the left support bearing end to the carriage, and almost no deformation occurs at the carriage; then, it increases and decreases to the right support bearing end. In addition, no transverse and bending vibration deformation occur at both ends of the support bearings, as shown in the picture. Fig. 8(b) represents the second-order vibration mode of the ball screw. The second-order vibration is represented by the coupled bending and transverse vibration of the lead screw. As the carriage moves away from the motor, the bending vibration amplitude of the carriage varies slightly, and the transverse vibration changes severely from the left end of the support bearing to about the center of the screw shaft. However, the bending vibration amplitude of the carriage varies greatly, and the transverse vibration changes slightly from about the center of the screw shaft to the right end of the support bearing. Fig. 8(c) represents the third-order vibration mode of the ball screw shaft. The third-order vibration is represented by the intense coupled bending and transverse vibration of the lead screw with the large vibration amplitude; the trend of the third-order vibration mode is similar to that of the second-order vibration. In addition, no transverse and bending vibration deformation occur at both ends of the support bearings, as shown in the picture.

Fig. 9 shows the first, third, and fifth order of the frequency changes of axial and torsional vibrations at different carriage positions and loads of the ball screw system. The load of the carriage is increased from 300 kg to 500 kg, and the carriage moves from the spot where is 0.25 *l* from left support bearing to 0.8 *l* of the screw shaft. The figure shows that the first-order axial vibration frequency increases with the position of the carriage close to the motor and decreases with the increase in the carriage load, with a maximum frequency variation range of approximately 10 %. The third-order vibration is the coupled axial and torsional vibration. The frequency is largely affected by the carriage position and slightly affected by the load of the carriage, and the maximum frequency range is approximately 50 %. The fifth-order vibration is mainly affected by the carriage load and hardly affected by the position of the carriage; moreover, in the middle of the screw shaft where stiffness is weakest, the frequencies decrease fast with the carriage load increase.

4. Conclusions

1) A novel model for ball screw feed systems was developed via the hybrid modeling method by considering the screw as a continuous body and the other parts as lumped mass bodies. On the basis of the Timoshenko beam assumption, the axial, torsional, transverse, and bending vibrations of the ball screw system are considered, and the Rayleigh-Ritz series method is used to establish the theoretical vibration model of the feed system; moreover, the frequency response characteristics and vibration mode shape of the ball screw are obtained. Results of the numerical simulation analysis and experiment show that the hybrid model can be used to study the dynamic characteristics of ball screw systems, especially the high-order modes, which can accurately characterize the flexible feature and coupling behavior of the lead screw.

2) Carriage position has a considerable influence on amplitude and direction of the axial and transverse vibration and a great influence only on the direction of the bending vibration; however, it has minimal influence on the amplitude and direction of the torsional vibration.

3) Carriage position and carriage load also have a great effect on the frequency response of the feed system. The first-order axial vibration frequency increases as the position of the carriage closes in to the motor and decreases as the carriage load increases. The third-order vibration frequency is largely affected by the carriage position and slightly affected by the carriage load. The fifth-order vibration is mainly affected by the carriage load and hardly affected by the position of the carriage; moreover, in the middle of screw shaft where stiffness is weakest, the frequencies decrease fast with the increase in carriage load.

Acknowledgements

This work was financially supported by the National Natural Science Fund of China (Grant No. 51765039 and No. 51965037).

Nomenclature

E : Young's modulus
G : Shear modulus
κ : Shear coefficient of the section
s : Lead of the ball screw shaft
J : Moment of inertia of the ball screw
J_m : Moment of inertia of the motor
J_c : Moment of inertia of the coupling
η : Damping loss factor
A : Cross-section area of the ball screw shaft
ρ : Density of the ball screw shaft
I_x : Moment of inertia of the cross section of the screw shaft around the x-axis
I_y : Moment of inertia of the cross section of the screw shaft around the y-axis
d : Diameter of the ball screw shaft
l : Length of the ball screw shaft
m_c : Weight of the table
k_{na} : Axial stiffness of the nut
k_{nr} : Radial support stiffness of the nut
k_b : Axial stiffness of the bearing
k_c : Torsional stiffness of the coupling
c_b : Damping coefficients of the bearing
c_n : Damping coefficients of the screw–nut interface
c_c : Damping coefficients of the coupling

References

[1] C. E. Okwudire and Y. Altintas, Effective simulation of ball screw drives modeled using finite element methods, *ASME Conference Proceedings*, 48753 (2008) 11-20.
[2] K. K. Varanasi and S. A. Nayfeh, The dynamics of lead-crew drives: low order modeling and experiments, *Journal of Dynamic Systems, Measurement and Control*, 126 (2004) 388-396.
[3] A. Diego et al., Modelling and vibration mode analysis of a ball screw drive, *International Journal of Advance Manufacture Technology*, 58 (2012) 257-265.
[4] L. Dong, W. Tang and L. Liu, Hybrid modeling and. time-varying analysis of vibration for a ball screw drive, *Journal of Vibration and Shock*, 32 (2013)196-202.
[5] Y. Yang, W. Zhang and H. Zhao, Dynamic characteristics of ball screw system, *Journal of Vibration, Measurement and Diagnosis*, 33 (2013) 664-727.
[6] J. S. Chen, Y. K. Huang and C. C. Cheng, Mechanical model and contouring analysis of high speed ball screw drive systems with compliance effect, *The International Journal of Advanced Manufacturing Technology*, 24 (2004) 241-250.
[7] M. S. Kim and S. C. Chung, Integrated design methodology of. ball-screw driven servo mechanisms with discrete controllers, Part I: modelling and performance analysis, *Mechatronic*, 16 (2006) 491-502.
[8] S. Fret, A. Dadalau and A. Verl, Expedient modeling of ball screw feed drives, *Production Engineering*, 6 (2012) 20-211.
[9] L. Wang et al., Nonlinear dynamic characteristics of NC table, *China Mechanical Engineer*, 20 (2009) 1513-1519.
[10] M. F. Zaeh, T. Oertli and J. Milberg, Finite element modelling of ball screw feed drive systems, *CIRP Annals-Manufacturing Technology*, 53 (2004) 289-292.
[11] R. Qian et al., Modeling and dynamic research based on Ritz series for ball screw drive system, *Journal of System Simulation*, 29 (2017) 2268-2275.
[12] H. Benjamin, S. Oliver and N. Rudiger, Distributed parameter modeling of flexible ball screw drives using ritz series discretization, *IEEE/ASME Transactions on Mechatronics*, 20 (2015) 1226-1235.
[13] Z. Lei et al., Hybrid dynamic modeling and analysis of a ball-screw-drive spindle system, *Journal of Mechanical Science and Technology*, 31 (2017) 4611-4618.
[14] C. Pislaru, D. G. Ford and G. Holroyd, Hybrid modelling and simulation of a computer numerical control machine tool feed drive, *Proc. Inst. Mech. Eng. I: J. Syst. Control, Eng.*, 218 (2004) 111-120.
[15] C. E. Okwudire and Y. Altintas, Hybrid modeling of ball screw drives with coupled axial, torsional, and lateral dynamics, *J. Mech. Des.*, 131 (2009) 071002.
[16] C. E. Okwudire, Improved screw-nut interface model for. high-performance ball screw drives, *J. Mech. Des.*, 133 (2011) 1009-1019.
[17] G. H. Feng and Y. L. Pan, Investigation of ball screw preload. variation based on dynamic modeling of a preload adjustable feed-drive system and spectrum analysis of ball-nuts sensed vibration signals, *Int. J. Mach, Tools Manuf.*, 52 (2012) 85-96.
[18] B. Bozyigit, Y. Yesilce and M. A. Wahab, Free vibration and harmonic response of cracked frames using a single variable shear deformation theory, *Structural Engineering and Mechanics*, 74 (2020) 33-54.
[19] B. Bozyigit,Y. Yesilce and M. A. Wahab, Transfer matrix formulations and single variable shear deformation theory for crack detection in beam-like structures, *Structural Engineering and Mechanics*, 73 (2020) 109-121.

[20] G, R. Gillich et al., Free vibration of a perfectly clamped-free beam with stepwise eccentric distributed masses, *Shock and Vibration* (2016) 2086274.
[21] B. Baran, Y. Yusuf and M. A. Wahab, Single variable shear deformation theory for free vibration and harmonic response of frames on flexible foundation, *Engineering Structures*, 208 (2020) 110268.
[22] P. Phung-Van, C. H. Thai and H. Nguyen-Xuan, An isogeometric approach of static and free vibration analyses for porous FG nanoplates, *European Journal of Mechanics / A Solids*, 78 (2019) 103851.
[23] V. Loc et al., Vibration analysis of cracked FGM plates using higher-order shear deformation theory and extended isogeometric approach, *International Journal of Mechanical Sciences*, 96-97 (2015) 65-78.
[24] I. Park and J. Park. Effective vibration test planning method for equipment with high slenderness ratio, *Journal of Mechanical Science and Technology*, 33 (12) (2019) 5779-5786.
[25] J. Hong, J. Kim and J. Chung, Stick-slip vibration of a moving oscillator on and axially flexible beam, *Journal of Mechanical Science and Technology*, 34 (2) (2020) 541-553, http://doi.org/10.1007/s12206-020-0102-y.

Qin Wu is a doctor of the School of Mechanical and Electrical Engineering, Lanzhou University of Technology, Lanzhou, China. She received her Ph.D. in Mechanical Engineering from Lanzhou University of Technology. Her research interests include mechanical vibration of CNC machine tools, nonlinear vibration and parameters identification.